Journal of Adhesion Science and Technology

ISSN: (Print) (Online) Journal homepage: https://www.tandfonline.com/loi/tast20

Effect of material positioning on Si-rich TIG welded joints of AA6082 and AA8011 by friction stir processing

Sipokazi Mabuwa, Velaphi Msomi, Husain Mehdi & Kuldeep Kumar Saxena

JOURNAL OF ADHESION SCIENCE AND TECHNOLOGY
2023, VOL. 37, NO. 17, 2484–2502
https://doi.org/10.1080/01694243.2022.2142366

Effect of material positioning on Si-rich TIG welded joints of AA6082 and AA8011 by friction stir processing

Sipokazi Mabuwa[a], Velaphi Msomi[a], Husain Mehdi[b] and Kuldeep Kumar Saxena[c]

[a]Mechanical Engineering Department, Cape Peninsula University of Technology, Bellville, South Africa; [b]Department f Mechanical Engineering, Meerut Institute of Engineering and Technology, Meerut, India; [c]Mechanical Engineering Department, GLA University, Mathura, India

ABSTRACT

The TIG-welded specimens were friction stir processed (FSPed) to analyze the impact material positioning of the base metals AA8011 and AA6082. The tests included the energy-dispersive X-ray spectroscopy (EDS), X-ray diffraction, microstructure, hardness, tensile test and fracture surface analysis. The mean grain size of 24.83 μm was obtained for the TIG welded joint, 8.68 μm for the FSPed joint with AA6082 alloy on the advancing side (A.S), while 11.14 μm was obtained when the AA8011 was positioned on the A.S. In the TIG + FSPed zone, an intricate vortex flow pattern could be seen. The extremely superplastic flow of plasticized material is seen in the mixed flow zone, which results in a tumultuous intercalation pattern. *In situ* extrusions of different alloys and severe plastic, deformation was induced by stirring tool action. Lamellae structure was generated by moving the plasticized material layer by layer. In this zone, vigorous mixing and penetration of A6082 and AA8011 were observed. The maximum tensile strength and strain rate of the TIG weldment showed a significant increase after friction stir processing from 83.83 MPa with a strain rate of 23.79% to 90.09 MPa with a tensile strain of 28.04. However, evaluating the FSPed joints, the AA8011-AA6082 specimen had better tensile properties. Moreover, the fracture surface analysis correlated with the tensile tests. The FSPed AA6082-AA8011 joint showed a higher hardness than the AA8011-AA6082 one.

ARTICLE HISTORY
Received 22 July 2022
Revised 3 September 2022
Accepted 22 September 2022

KEYWORDS
Microstructure; dynamic recrystallisation; tensile properties; microhardness; fractography

1. Introduction

Aluminium alloy AA8011-H14 is a wrought alloy with an H14 temper. This aluminium alloy grade is strain hardened to a strength roughly between the annealed (O) and the entire hardened grade H18 [1]. The AA8011-14 is sometimes referred to as the Al–Fe–Si due to the aluminium, iron and silicon elements [2]. The AA8011 grade is mainly used in ventilation and fins of heat exchangers, aerospace and outdoor electrical

CONTACT Husain Mehdi husainmehdi4u@gmail.com Department of Mechanical Engineering, Meerut Institute of Engineering and Technology, Meerut, India.

cabling industries [3]. This alloy harbours properties like attractive reflective physical appearance, good formability, good machinability, good weldability, good corrosion-resistant and lightweight [1–3]. Aluminium alloy AA6082 is a heat-treated solution, stress relieved by artificial age and stretching. AA6082-T651 has the lowest ductility compared to the other variations of 6082 aluminium [4]. This grade is sometimes called the Al–Mg–Si due to the aluminium, magnesium and silicon dominance [5,6]. The AA6082-T651 alloy consists of medium strength, excellent corrosion resistance, good workability, good weldability and machinability.

AA6082-T651 is utilized in bridges, cranes, trusses and aerospace engineering. The AA6082 replaces the AA6063 and AA6061 in the automobile and aircraft industries [7].

The ever-changing technology suggests the production of new structures and components from various materials and alloys. This is evident in the products used daily, which are made from multi-materials to increase the functionality and flexibility of the design [8]. This suggests the possibility of new components and surfaces being formed from the two mentioned aluminium alloys. Both aluminium alloys have good weldability, which makes welding a possible technique that can be used for joining these two together. The worldwide welding techniques include gas metal arc welding (GMAW), tungsten inert gas welding (TIG) and the emerging solid-state called friction stir welding (FSW) technique are the most used methods for joining soft materials. However, the TIG welding technique has been the most preferred technique over the GMAW technique due to the possibility of obtaining high joint strength [9–11]. However, the drawbacks of joining dissimilar alloys cannot be ignored. Various drawbacks of dissimilar alloy welding include high residual stresses, solidification cracking, porosities and brittle intermetallic compounds resulting in poor mechanical characteristics [12,13]. The mentioned drawbacks reduce weld strength, which can be eliminated through the variant of FSW called friction stir processing (FSP). This process provides a homogenous refined grains structure in the near-surface layers of the processed metals. The application of FSP results in homogeneity and microstructure refinement of the FSPed region due to good material mixing, plastic deformation and thermal exposure. This FSP method has been successfully employed in modifying microstructure and in-situ surface composites [14]. Numerous works have investigated the FSP technique's impact on TIG welded joints. This includes Mabuwa and Msomi [15], where the FSP method was applied on the TIG welded AA5083 alloy joints to analyze the changes in metallurgical properties of the weldments and revealed that the microstructural grain sizes of the nugget zone (NZ) were reduced from 10.78 to 7.18 µm. This grain refinement was reported to have increased ultimate tensile strength (UTS) from 153.75 to 249.92 MPa and joint percentage elongation from 16 to 22.86%. Mishra and Mehdi [16] have also investigated the effect of employing FSP on TIG-welded aluminium alloy AA6083-T6 and AA2024. Applying FSP to the said joints resulted in the elimination of coarse grains to more refined grains. The hardness of FSPed TIG welded joints was significantly improved compared to the TIG weldments [17]. The microstructural grain sizes in the NZ of the FSPed TIG joints were significantly reduced from 19.8 to 4.2 µm. The tensile test results revealed that FSP enhanced the mechanical characteristics of the weldments, where the highest UTS of 255 MPa was achieved [18]. Similarly, due to the grain size modification, the FSPed joints were more ductile than the TIG weldments. Abbasi et al. [19] analyzed the friction stir vibration, and the FSP method enhanced the metallurgical characteristics of the TIG weldments of AA5052 and demonstrated that both FSP methods were influential in the grain size refinement, which enhanced the ductility (22%) and UTS (10%) in the processed area. An increased fraction of high angle grain boundaries post-FSP application on the TIG welded joints was seen in the TIG + FSP welded joints of AA7075 [20]. Additionally, the dendritic structure on the TIG weldments disappeared after FSP, and refined equiaxed grains were reported. The process parameters of FSW enhanced the mechanical properties of the similar and dissimilar welded joints. They displayed superiority in the FSWed joints regarding adaption to optimized process parameters, modern technologies and the ability to join various similar and different alloys [21]. The cited studies show that the FSP technique can improve various properties of the TIG welded joint. However, the improvement of joint properties relies mainly on the process parameters, especially when the processing involves dissimilar materials. This paper is focused on analyzing the impact of material positioning on the tensile characteristics of the FSPed TIG-weldments. This work was undertaken due to little or no available work on the importance of material positioning during the FSP of dissimilar TIG weldments.

2. Materials and methods

The base metal used AA8011 and AA6082 alloys plate dimensions 200 × 60 × 6 mm in this work. Tables 1 and 2 demonstrate the chemical compositions of the base metals and filler ER4043, which were analyzed by the Belec Compact Port HLC machine. The chemical compositions agreed with those obtained in the literature [22–25]. The mechanical characteristics of the AA6082 included a UTS of 308 MPa, % elongation of 25.42% and a hardness of 89.6 HV, while those of the AA8011 had a UTS of 94.1 MPa, elongation of 40.17% and a hardness of 33.5 HV [26]. The acetone was employed to remove the dust and other contaminations on the plate surface before the TIG welding. The oxide layer was removed using the steel wire brush. The JAVWELD TIG welding machine was used for welding the dissimilar alloys. The filler ER4043 with a diameter of 2.4 mm was used to join the double V-groove joints. The TIG welding parameters used during the process as demonstrated in Table 3. Three sets of the plates were

Table 1. Chemical compositions of base metals.

	Mg	Zn	Ti	Cr	Si	Mn	Fe	Cu	Al
AA8011-H14	0.441	0.074	0.015	0.038	0.515	0.556	1.033	0.09	Bal
AA6082-T651	1.24	0.941	0.044	–	1.063	0.356	0.899	0.045	Bal

Table 2. Wire filler chemical composition.

	Si	Fe	Zn	Mg	Ti	Cu	Al
ER4043	5.442	0.782	0.11	0.052	0.022	0.025	Bal

Table 3. Process parameters of TIG welding [27].

Voltage (V)	Shielding gas	Current (Amps)	Gas flowrate (L/min)	Welding speed (mm/min)
35	Argon	115	6	40

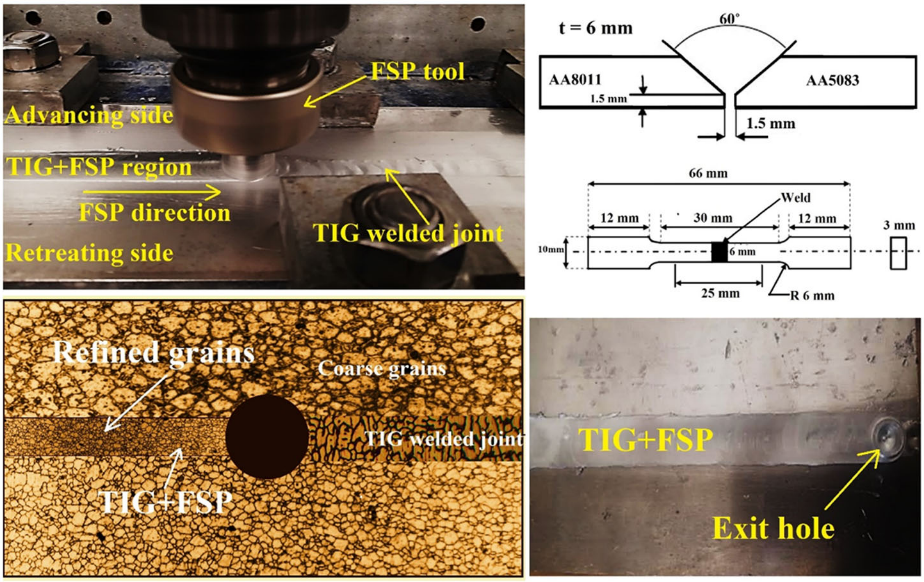

Figure 1. Experimental representation of TIG and TIG + FSP welded joints.

TIG-welded. One was kept for comparison, the second one was set for FSP with the AA8011 side on the A.S and AA6082 on the retreating side (R.S), and the third set AA6082 side was positioned on the A.S with AA8011 on the R.S. The semi-automated vertical milling machine, LAGUN FU.1-LA model was employed for FSP. The FSP process parameters included a welding speed of 55 mm min^{-1}, a penetration depth of 5.7 mm, rotational tool speed of 1200 rpm [28] with a tilt angle of 2°. A triangular cross-section pin was employed in this work because it revealed fine and homogenous dissemination of grains in the stir zone which exhibits the excellent mechanical properties of the welded region [29,30]. A triangular cross-section pin made of high-speed steel in which the tool pin diameter was 7 mm, tool pin length was 5.7 mm, and tool shoulder diameter was 20 mm. The application of the FSP technique on the TIG weldments is depicted in Figure 1. It should be noted that three specimens were initially tested for each joint produced; for this study, one specimen with better results was chosen from each.

The Weck's etchant with a composition of 1 g of sodium hydroxide, 4 g of potassium permanganate and distilled water was immersed in the specimens for 15 s. The modified Keller's etchant composed of 10 ml of HNO_3, 1.5 ml of HCL, 1.0 ml of HF and 87.5 ml of distilled water was applied after the Weck's etchant for 20 s. The Motic AE2000 metallurgical light optical microscope examined the grain structure and the Tescan scanning electron microscope (SEM). The ASTME112-12 standard was employed to analyze the average microstructural grain sizes of the nugget zone [31,32]. To analyze the grain size, the linear intercept method was employed by ImageJ software. The Vickers microhardness of the specimens was analyzed using Innovatest Falcon 500 hardness machine based on the ASTME384-11 standard [31,32]. The load of 300 g and the dwell time of 10 s were applied. There were 16 indentations with a

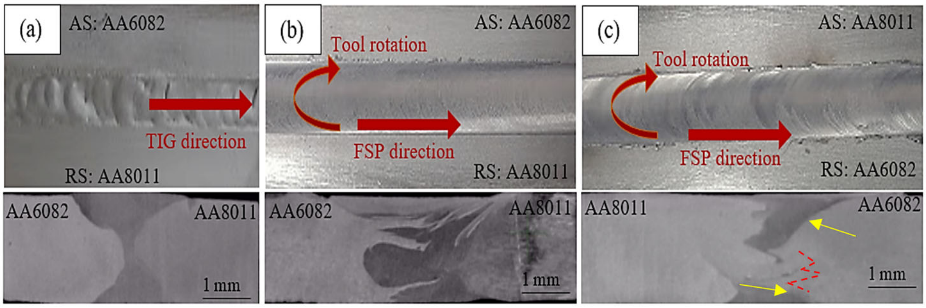

Figure 2. Surface macrographs, (a) TIG welded, FSPed-TIG welded (b) AA6082-AA8011 and (c) AA8011-AA6082.

1 mm spacing used for each sample. The uniaxial tensile test was conducted using the ASTM E8M-04 standard [31,32] through the Hounsfield 50 K tensile testing machine.

3. Results and discussion

3.1. Macrostructural analysis

The macrographs with overall surface appearance produced from the TIG welded and FSPed-TIG welded joints are shown in Figure 2. The TIG welded shows a good weld with no visible pores on the surface and structure. Both FSPed joints revealed a good quality weld structure with no defects. No visible flash was noted on the AA6082-AA8011 weld, while the AA8011-AA6082 showed minimal flash. Further examination of the macrostructure cross-sections revealed that the NZs consist of a probe-affected zone and a shoulder-affected zone. These zones resulted in the formation of a crown-like zone which is formed in the transverse direction. The onion ring-like structures were observed on the AA6082-AA8011 joints with a circular flow pattern. The circular flow pattern results from the bright and dark lamellae of the dissimilar aluminium joints [33,34]. It was observed that the AA6082 alloy was plastically deformed and dominated in the NZ. The AA8011-AA6082 joint macrograph in Figure 2(c) showed a smaller NZ due to AA8011 having a lower viscosity than AA6082 alloy at higher temperatures [33]. A zigzag-like nugget shape shown by the red lines was noted. Along the zigzag, the presence of the ER4043 filler demonstrated by the yellow arrows was observed. This could mean that the dissimilar alloys and the ER4043 filler didn't thoroughly blend during the mixing and deformation of the joints.

3.2. Microstructural analysis

In the TIG + FSP, the base material on the A.S. is much high penetratingly elated around the rotating tool before being deposited in the FSPed joints suggested by Park et al. [2], observed that the base metals were more appropriately mixed when the AA6082 was on the A.S. than in the case of AA8011. The various onion rings were seen in the N.Z., mainly when the AA6082 was located on the A.S., The process of the many onion rings was assumed to correlate to the FSW tool's thread pitch. Figure 3 shows the intricate materials flow patterns on the upper A.S. and R.S., as well as the

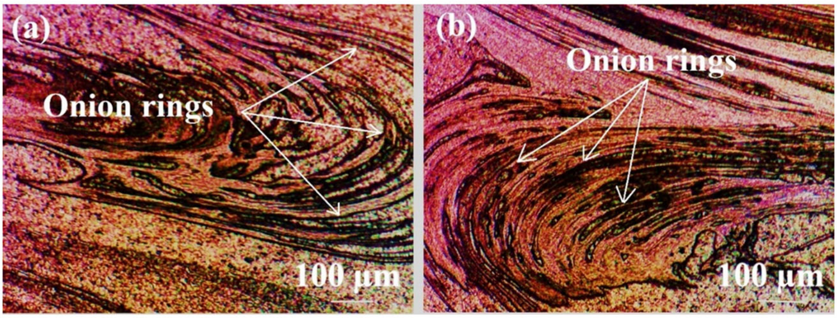

Figure 3. Onion rings in TIG + FSP welded joints, (a) AA8011-AA6082 joint, (b) AA6082 and AA8011.

many onion rings in the N.Z. Three sub-layers may be seen in the FSWed joints of AA8011 and AA6082, such as (a) AA8011 sublayer, (b) AA6082 sublayers and (c) mixing of sublayers of base metals. The plasticized materials in the regions close to the flats may have encountered significant extrusion turbulence and had enough time to be well mixed before eventually being deposited into the wake of the FSWed joints, which might explain the formation of the mixed sub-layers. AA6082 and AA8011 alloys that have been plasticized were mechanically connected. Partial penetration of AA6082 and AA8011 has been achieved. However, the DRX of grains was obvious. Both alloys have alternate lamellae in the mixed flow zone. In the TIG + FSPed area, an intricate vortex flow pattern could be seen. The extremely superplastic flow of plasticized material is seen in the mixed flow zone, which results in a tumultuous intercalation pattern. *In situ* extrusions of different alloys and severe plastic, deformation were induced by stirring tool action. Lamellae structure was generated by moving the plasticized material layer by layer. In this zone, there was vigorous mixing and penetration of A6082 and AA8011. Due to their various etching reaction to the Keller's reagent, the AA6082 was seen as dark, while the AA8011 alloy was lighter in colour. The material's mixing appears to be significantly more successful when the AA6082 is placed on the A.S., particularly at a higher welding speed [1]. During FSP, microstructure observation is commonly employed to identify such defects as tunnelling defects, pinholes, fractures, etc. But at lower magnification, various minor defects could not be observed, so high magnification analysis is required. Figure 3 depicts the microstructure of the TIG + FSPed joints of AA8011 and AA6082 generated at various parameters. A combination of three factors forms FSPed joints. The first is a plastic material stirring, which collects the plasticized multi-layer materials behind the FSP tool and is affected by an interplay of traverse speeds, pin profile and TRS. The second is a rise in temperature in the welded zone, which softens the parent material in the N.Z. The third is the hot forging of plasticized material by the FSP tool shoulder. The defective FSPed region would be found if any improper adjustment of these parameters occurred.

Figure 4 reveals the optical micrographs of the TIG weldment of different zones. The optical micrographs of the welded joints were classified into three distinct regions, the heat-affected zone (HAZ), the partially melted zone (PMZ) and the fusion zone (FZ). The HAZ region depicted in Figure 4(a,d) clearly shows a coarse grain structure and grown epitaxial dendritic grains near the weld interface. This region is where the

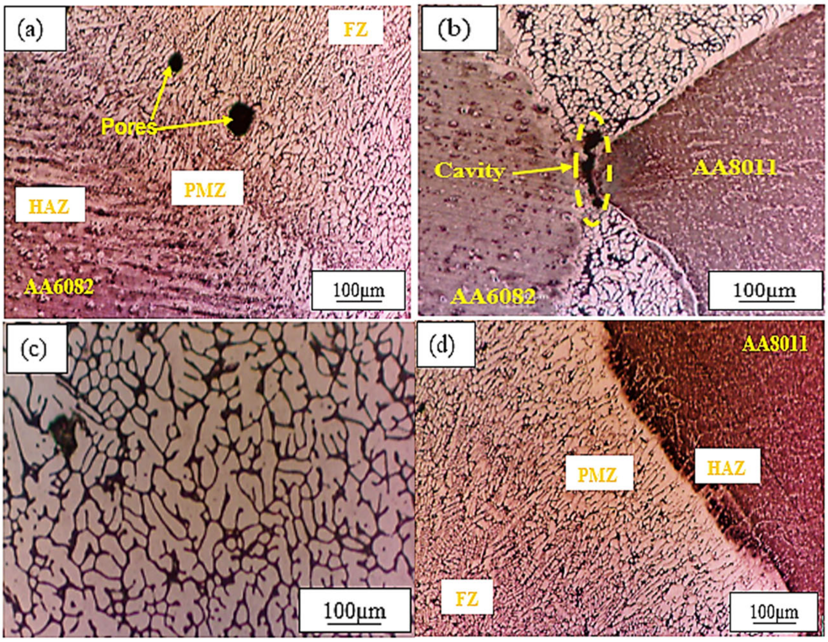

Figure 4. TIG-welded joint micrograph, (a) HAZ, PMZ and FZ on the AA6082 side, (b) centre of the weld (c) FZ and (d) HAZ, PMZ and FZ on the AA8011 side.

specimens mostly fail since it is where the HAZ softening phenomenon occurs, making it the weakest position [27]. The PMZ was formed from the HAZ coarse grains. The PMZ is between the HAZ and the FZ. The PMZ consists of the coarser recrystallised grains caused by partially melting the grain boundaries [35,36].

In the PMZ, the parent hardened precipitates undergo heat treatment over ageing, resulting in phase formation and weakening the welded area's mechanical properties [37]. Figure 4(b) reveals the centre of the TIG welded joints, where the two aluminium alloys meet. The FZ micrograph of the TIG-welded specimen illustrated in Figure 4(c) reveals both epitaxial growth and columnar grain structure. In the FZ, epitaxial nucleation and growth dictate the microstructural evolution [36]. Figure 4(a–c) showed defects in pores and cavities, as illustrated by the yellow markings. The presence of the said defects affects the tensile characteristics of the weldment negatively. The formation of the defects arises from the TIG welding wire and absorption of the shielding gas in the molten pool, which is then released on the solidification and trapped in the weld metal [38].

The FSPed-TIG welded joints micrographs illustrated in Figure 5 revealed HAZ, thermomechanical affected zone (TMAZ) and the NZ. The modification of the coarse and columnar grains noted in the FZ of the TIG weldment occurred in the HAZ and TMAZ, as demonstrated in Figure 5(a,b) and (d,e), respectively. Figure 5(c,f) in the NZs depicted fine equiaxed recrystallised grain structures. During the joints ' processing, the maximum plastic deformation caused these grain structures [15,39]. A tunnel defect was also not noted on the FSPed-TIG welded joint in Figure 5(e). The tunnel defect formation is associated with inadequate heat generation to melt both materials [40].

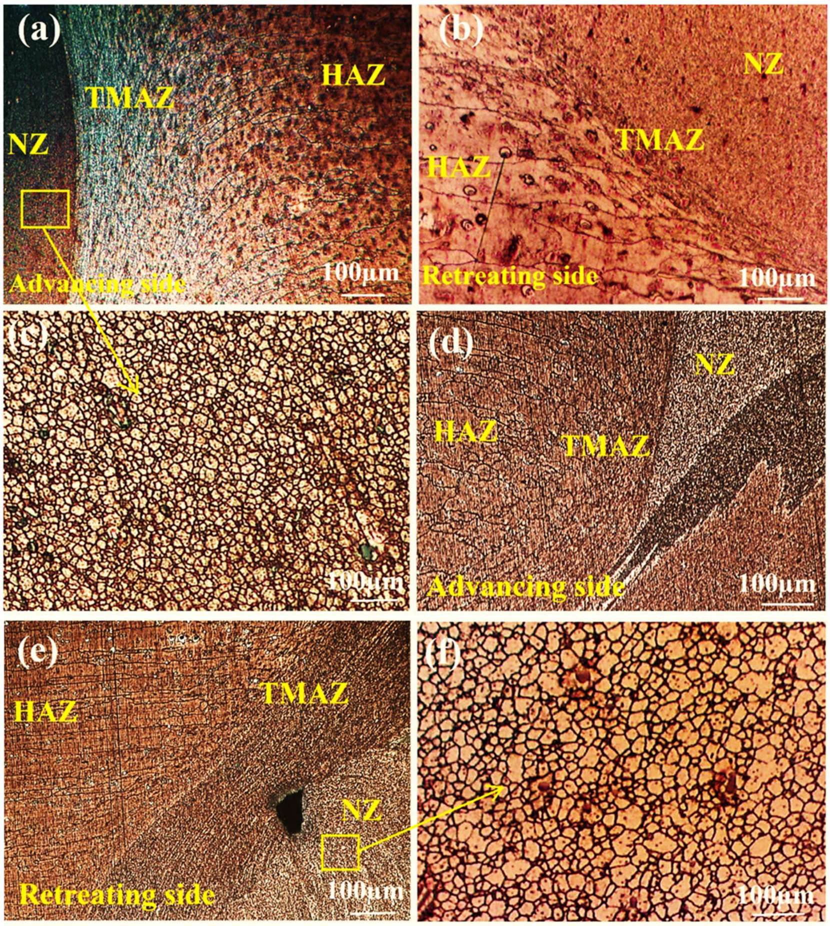

Figure 5. optical microstructure of the FSPed joints, (a) Advancing side of the AA6082-AA8011 joint, (b) Retreating side of the AA6082-AA8011 joint, (c) Nugget zone of the AA6082-AA8011 joint, (d) Advancing side of the AA8011-AA6082 joint, (e) R.S of the AA8011-AA6082 joint, (f) Nugget zone of the AA8011-AA6082 joint.

Table 4. Mean grain size and standard deviation.

Joint	Mean grain size (μm)	Standard deviation (μm)
TIG-welded FZ	24.83	7.62
FSP TIG (AA6082 advancing) NZ	8.68	3.12
FSP TIG (AA8011 advancing) NZ	11.14	3.46

Table 4 shows the grain sizes of the TIG and TIG + FSPed joints. The parent material means grain sizes were previously determined where the AA6082 was 64.04 μm, and the AA8011 was found to be 51.57 μm [41]. The TIG-welded joint mean grain size was 24.83 μm which is less than the parent materials. Post FSP of the TIG weldments; the grain structure was significantly fine, and the average grain size of 8.68 μm for the joints with AA6082 on the A.S and 11.14 μm with AA8011. The grain sizes resulted from the dynamic recrystallisation, severe heat and maximum plastic deformation [14, 18, 39]. The joint with a maximum UTS parent material on the A.S (AA6082-AA8011)

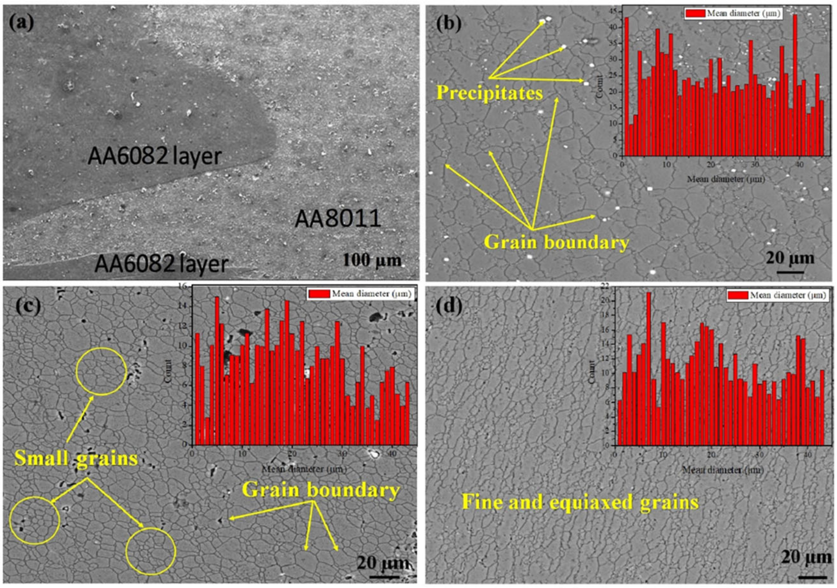

Figure 6. SEM images with grain distribution bars, (a) mixing of AA6082 and AA8011, (b) TIG-welded FZ, (c) FSPed-TIG-welded NZ (AA6082-AA8011 joint) and (d) FSPed-TIG-welded NZ (AA8011-AA6082 joint).

possessed a more refined grain structure and mean grain size than the joint with lower strength alloy on the A.S (AA8011-AA6082). This behaviour was also reported in the literature [42–44]. This phenomenon is due to the material placed on the advanced dominating the NZ and respective material plastic flow [43]. Likewise, it should be seen that when the AA8011 was positioned on the A.S, the material reached a melting point faster than the higher strength alloy. This, therefore, resulted in the softening of the joint with AA8011 on the A.S, while within the same joint, there are possibilities of the cold weld formed due to the AA6082 not melting simultaneously with the AA8011 alloy. Additionally, the material positioning dictates the temperature gradient, which significantly influences the microstructural grain size [45]. The matching grain size distribution with respective joints is demonstrated in Table 4 and Figure 6.

Figure 6 demonstrates the fine grain structure in the NZ in TIG + FSPed samples due to dynamic recrystallization (DRX) and grain stirring. The TMAZ region was also observed with refined grains compared to the HAZ region, associated with moderate strain rate and thermal cycle. From the weld centre to the parent metal, the temperature experiences varying degrees of plastic strain. Material close to the NZ experiences a significant degree of plastic strain, which raises the temperature relative to the other zone (TMAZ and HAZ). A heterogeneous microstructure develops due to the heterogeneity of the temperature plastic strain. Due to the DRX, the NZ noticed the structure of refined and equiaxed grains, and this DRX was caused by plastic deformation combined with a high temperature [3]. The NZ experiences extreme heat, which causes the grains to recrystallize while different grains undergo nucleation. The rotating tool broke them up into little, evenly spaced grains. The temperature of the upper NZ was relatively high because the bottom NZ heat could quickly transfer to the base plate and

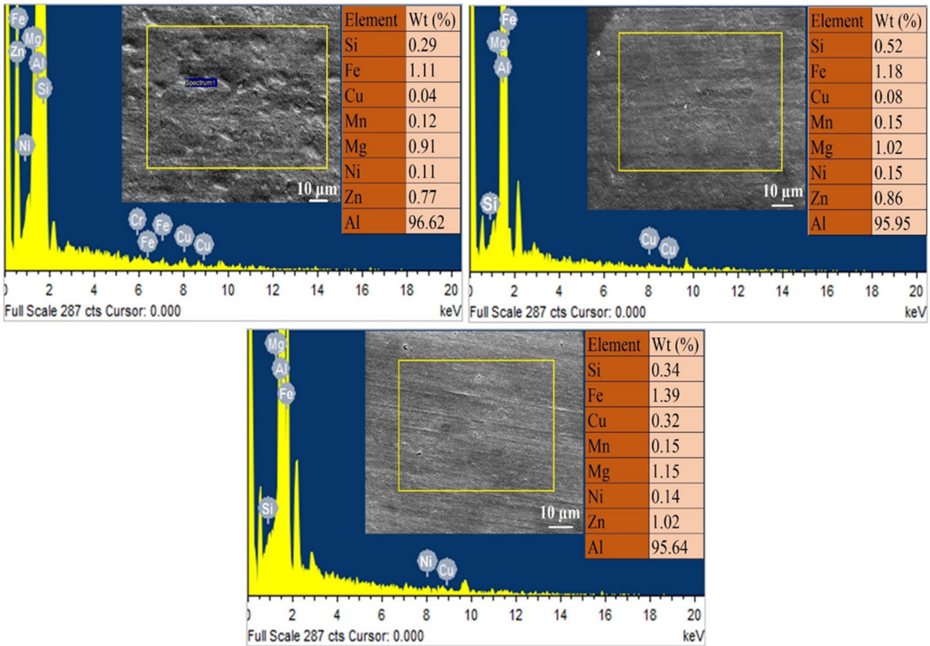

Figure 7. EDX images, (a) TIG-welded FZ, (b) FSPed-TIG-welded NZ (AA6082-AA8011 joint) and (c) FSPed-TIG-welded NZ (AA8011-AA6082 joint).

backing plate. With the lower temperature, the grains in the bottom NZ have less time to grow up. Due to high stacking fault energy, the FSWed joints may experience continuous DRX and discontinuous DRX in the hot deformation process [4]. In the NZ, many equiaxed and fine grains were observed in the NZ of TIG + FSP weldments. The high peak temperature associated with plastic deformation facilitates the DRX, which results in high-angle grain boundaries with recrystallized and fined grains in the NZ. The original grains in the NZ undergo extrusion action of the tool shoulder under the distortion deformation. Many broken grains remain in the NZ due to high thermal gradient and high strain from the tool shoulder to the upper surface of the TIG + FSPed weldments of AA6082 and AA8011, resulting in the development of dense sub-grains boundary [5,6].

Figure 7 demonstrates the EDS of TIG and TIG + FSP weldments of AA8011 and AA6082, where the Al and Fe percentage in the welded region was higher than the other element. In TIG welded joint, the aluminium percentage (96.62%) is the maximum, Fe is the 2nd maximum (1.11%) and Mg is the 3rd maximum (0.91%). The alloying elements were homogeneously disseminated in the TIG + FSP region, enhancing the welded joints' mechanical properties. The principal alloying elements were more evenly distributed in the NZ during TIG + FSP welded joints revealed in Figure 7.

3.3. X-ray diffraction (XRD) analysis and chemical composition of joints

It was observed that there was high Fe content on the FSPed joints compared to the TIG weldment. This is presumed to be due to the position where the probe scanned

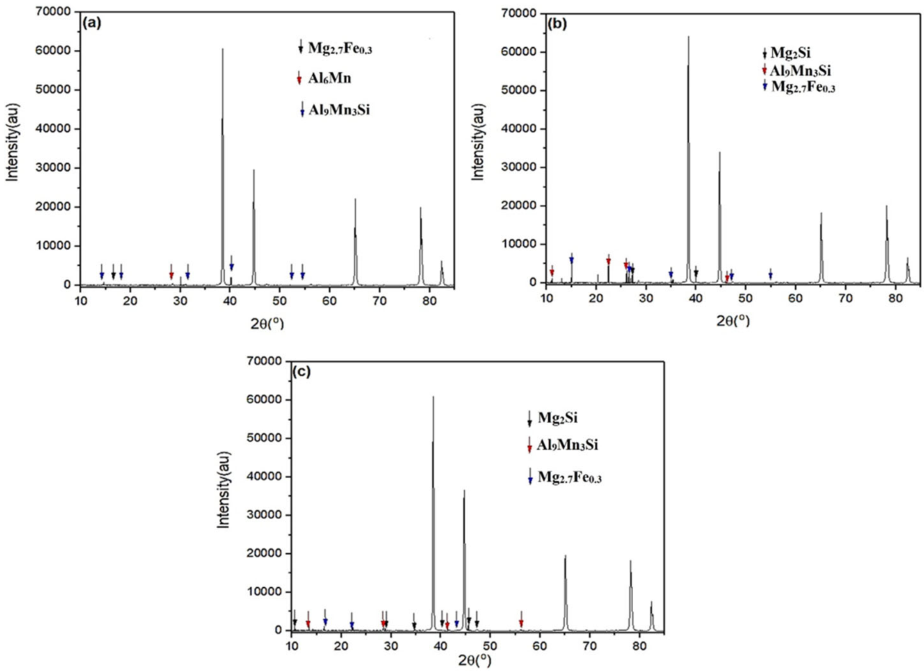

Figure 8. XRD peaks, (a) TIG, (b) FSPed-TIG AA6082-AA8011 joint, (c) FSPed-TIG AA8011-AA6082 joint.

the chemical data being likely filled with more AA8011 alloy than the AA6082 one. The AA8011 has a very high content of Fe compared to the TIG welded joint, which is dominated by the filler metal content. Figure 8 revealed the XRD peaks of the TIG-welded FZ and FSPed TIG-welded NZs for the dissimilar joints of AA8011-AA6082 and AA6082-AA8011. The XRD was conducted to examine the phase detection of the said joints. Several phases were detected in joints of different specimens. Figure 8(a) shows the phases detected on the TIG-welded joint. Various phases were seen from the TIG welded, and these phases do not play a significant role in the strengthening mechanism. It was perceived that the Mg_2Si phase was not detected in this joint, and its disappearance is attributed to the high operating temperature associated with the TIG welding technique [25,26,28,29]. It was anticipated that the Mg_2Si be absent from the TIG welded joint because there was a notable drop in Mg and Si content in the chemical composition of the joint. There was a noteworthy increase in Mg and Si content in the joint post-FSP procedure; hence Mg_2Si phase was detected in Figure 8(b,c). It should be noted that the unlabelled peaks on the XRD results represent the aluminium phase. Other phases were detected from the specimens, but their presence was insignificant compared to the precipitate called Mg_2Si.

3.4. Hardness distribution analysis

The maximum hardness obtained for the TIG welding FZs was 78 HV. The maximum hardness for the FSPed TIG-welded NZ was 67 HV for the AA6082-AA8011 joint and 58 HV for the AA8011-AA6082 one. The FZ hardness of the TIG welded was more

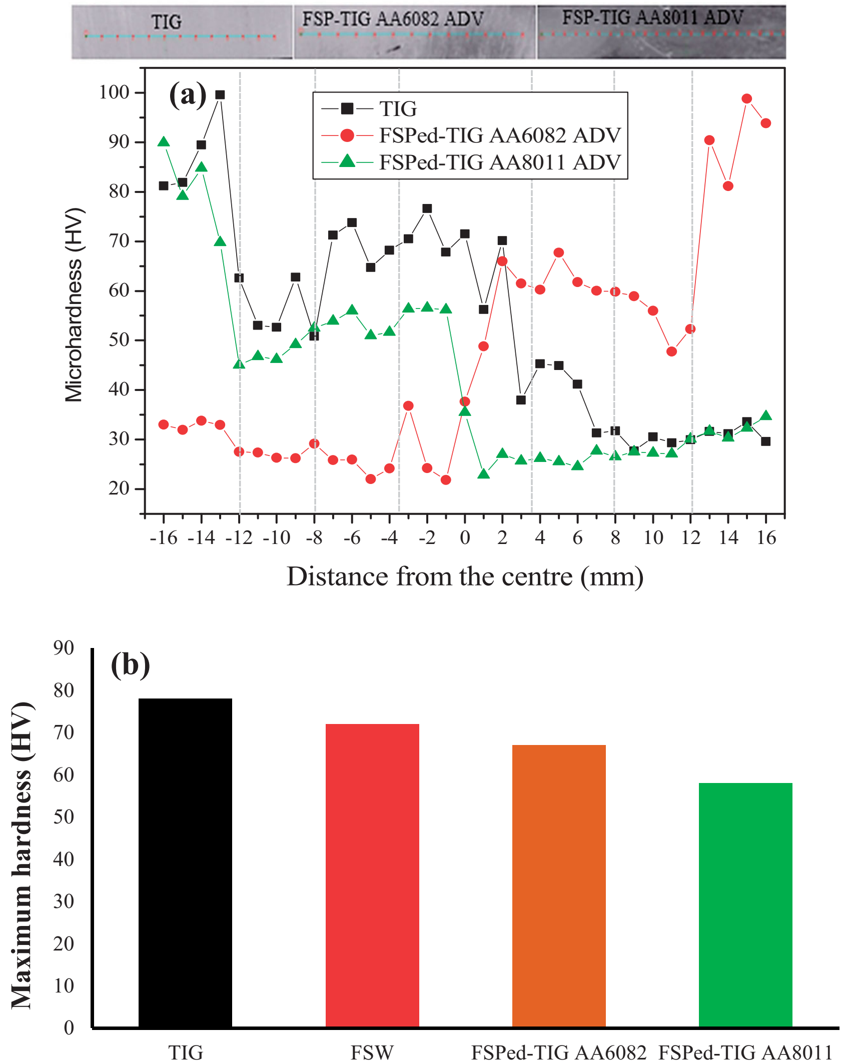

Figure 9. (a) Microhardness distribution profiles of the joints, (b) Maximum hardness of the joints.

significant than the NZ hardness of the FSPed joints. The lower hardness of FSPed joints was caused by the excessive heat that the joints experienced while subjected to TIG welding and FSP. At the same time, the TIG welded joint only experienced single heat during the welding process. The joint was affected by heat experienced due to the AA6082 alloy being susceptible to temperatures above 200 °C since it is a precipitate-strengthened alloy. The strengthening precipitates dissolve in high temperatures experienced during the welding or processing, resulting in decreased joint hardness and mechanical properties [46,47]. The XRD analysis further confirms this. Both TIG welded and FSPed-TIG welded joints had lower NZ hardness than the AA6082 parent material but higher NZ hardness than the AA8011 parent material. The hardness decreased from mixing the AA6082 alloy with a lower hardness alloy, AA8011. Comparing the NZ hardness of the FSPed joints, the AA6082-AA8011 had a higher

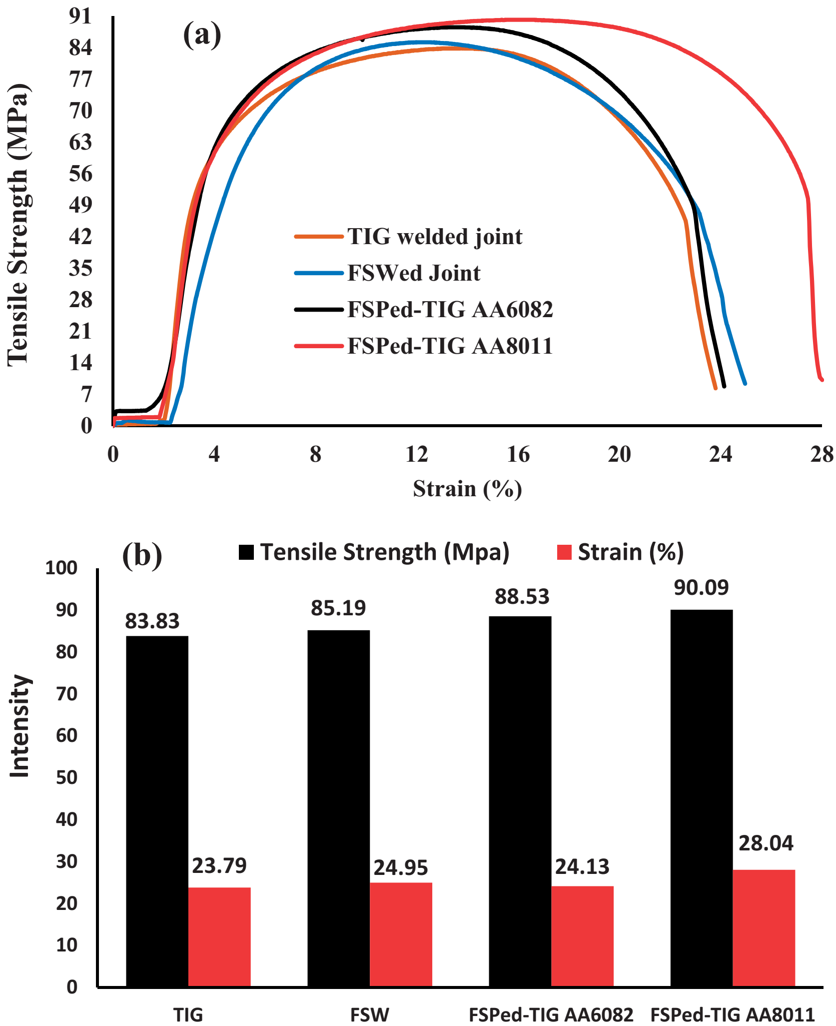

Figure 10. (a) Tensile stress and strain curves, (b) Comparison of ultimate tensile stress and strain for the joints.

hardness than the AA8011-AA6082. This behaviour correlates with the microstructural grain sizes obtained, and strengthening precipitates were detected post FSP procedure. Similar studies with similar behaviour where the positioning of the high strength-parent material on the advancing yielded better hardness than when the lower strength alloy was positioned on the A.S were recorded [42,48–50].

The hardness distribution was evaluated on the transverse cross-section of the weldments. Figure 9(a) illustrates the hardness results of the TIG and TIG + FSPed weldments. Figure 9(b) shows the maximum hardness results of the joints presented in Figure 9(a). The average parent material hardness value for the AA6082 was 89 HV and 35 HV for the AA8011 parent material. The PMZ hardness on the AA6082 side for TIG welded joints was noted to have higher hardness compared to that of the FZ of the same joint. Similar observations were observed on the TMAZ of both FSPed joints

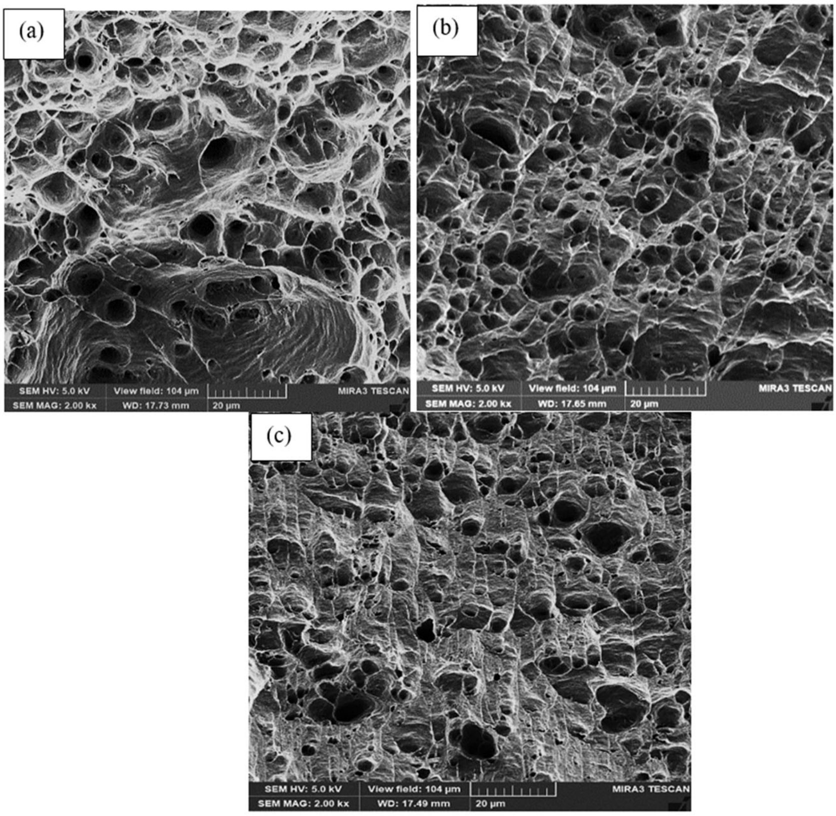

Figure 11. SEM tensile fractographs, (a) TIG welded joint, (b) FSPed-TIG welded AA6082-AA8011 joint, (c) FSPed-TIG welded AA8011-AA6082 joint.

compared to the NZs. The behaviour is assumed to be because the dissolution of the precipitates in the PMZ and TMAZ is not likely to happen due to temperature differences compared to the FZ or NZ [42].

3.5. Tensile properties

The stress–strain diagram for the TIG, FSW weldment and FSPed joints is shown in Figure 10(a). The TIG-weldments fractured on the AA8011 HAZ due to the region's lower hardness and weakened mechanical properties. Similar behaviour was also noted on the FSPed-TIG welded joints. The maximum UTS of the TIG welded was increased from 83.83 to 90.09 MPa after FSP, while tensile strength of the FSW was observed as 85.19 MPa. The improvement in UTS is caused by eliminating porosities initially present on the TIG welded joints and the refinement of the larger columnar grains by FSP [15,18]. This UTS behaviour correlated with the grain sizes obtained. This behaviour was in line with the Hall-Petch relationship [51]. However, comparing the FSPed TIG-welded maximum UTS, the AA6082-AA8011 had a UTS of 88.53 MPa, and 90.09 MPa was obtained for the AA8011-AA6082 joint. The AA8011-AA6082 was noted to have a higher strain rate of 28.04%. This was caused by the AA8011 alloy positioned on the A.S having a high ductility compared to the AA6082 alloy. This substantiation agrees with the literature where both parent materials were subjected to axial tensile testing; the AA8011 showed a significantly higher ductility [52]. The TIG-welded joint had a lower strain rate than both FSPed joints, as depicted in Figure 10(b).

3.6. Fracture surface analysis

The SEM fractography of the TIG and TIG + FSPed joints of AA8011 and AA6082 was depicted in Figure 11. The TIG-welded specimen failed TIG-welded of the AA8011 parent material. The FSPed samples also failed on the HAZ of the A8011 on the R.S of the AA6082-AA801 joint) and on the A.S of the AA8011-AA6082 joint. This is due to the hardness, and the coarse grain structure found on the HAZ and the AA8011 being a low-strength alloy [39,53]. The joints showed ductile failure characteristics such as dimples, microvoids, facets and grain boundaries [25]. The TIG-welded fractography showed more enormous dimples with bigger microvoids and facets. The FSPed AA6082-AA8011 joint showed a coalescence of microvoids with fine equiaxed dimples, and the AA8011-AA6082 joint showed sheared and spherical dimples. The AA8011-AA6082 dimples confirm the high ductility.

4. Conclusions

The correlative analysis of material positioning and metallurgical characteristics of the FSPed-TIG-welded joint of AA8011 and AA6082 was successfully executed and found the following conclusions.

- The maximum hardness obtained for the TIG welding FZs was 78 HV. The maximum hardness for the FSPed TIG-welded NZ was 67 HV for the AA6082-AA8011 joint and 58 HV for the AA8011-AA6082 one. The FZ hardness of the TIG welded was more significant than the NZ hardness of the FSPed joints.
- The maximum tensile strength and strain rate of the TIG weldment showed a significant increase after friction stir processing from 83.83 MPa with a strain rate of 23.79% to 90.09 MPa with a tensile strain of 28.04.
- Lamellae structure was generated by moving the plasticized material layer by layer. There was vigorous mixing and penetration of A6082 and AA8011. The material's mixing appears to be significantly more successful when the AA6082 is placed on the A.S.
- The FSPed-TIG welded joints had lower NZ hardness than the TIG welded joint and AA6082 parent material but higher NZ hardness than the AA8011 parent material. The application of FSP on the TIG weldment was found to have a minimal increase in the UTS and a significant increase in the tensile strain rate. The fracture surface analysis correlated with the tensile tests. The fractography of the FSPed joints showed more ductile features than the TIG welded one.
- The microstructural grain sizes post-FSP of the TIG weldments were significantly reduced regardless of material positioning. The joint with a higher strength parent material on the A.S (AA6082-AA8011) showed more refined grains than the joint with lower strength alloy on the A.S (AA8011-AA6082). The XRD patterns

post-FSP revealed the strengthening precipitate Mg_2Si, which was not detected on the TIG weldments. Other phases seen on the FSP joints included the Al_9Mn_3Si and $Mg_{2.7}Fe_{0.3}$.

Acknowledgments

The authors express heartfelt thanks to Department of Mechanical engineering, Cape Peninsula University of Technology, South Africa for providing the experimental setup and their corresponding labs for supporting this work.

Author contributions

Sipokazi Mabua, and Velaphi Msomi: Conceived and planned the experiments, reviewing and carried out the experiments. Husain Mehdi: Paper writing, reviewing and editing. Kuldeep Kumar Saxena: Reviewing and editing

Disclosure Statement

No potential conflict of interest was reported by the author(s).

ORCID

Husain Mehdi http://orcid.org/0000-0003-4191-0142
Kuldeep Kumar Saxena http://orcid.org/0000-0003-4064-5113

References

[1] Totten GE, Mackenzie DS. Handbook of aluminum. Vol. 2, Alloy production and materials manufacturing. Basel: Marcel Dekker, 2003.
[2] Wahab Hashmi A, Mehdi H, Mabuwa S, et al. Influence of FSP parameters on wear and microstructural characterization of dissimilar TIG welded joints with Si-rich filler metal. Silicon. 2022. https://doi.org/10.1007/s12633-022-01848-8.
[3] Salah AN, Mabuwa S, Mehdi H, et al. Effect of multipass FSP on Si-rich TIG welded joint of dissimilar aluminum alloys AA8011-H14 and AA5083-H321: EBSD and microstructural evolutions. Silicon. 2022. https://doi.org/10.1007/s12633-022-01717-4.
[4] Dursun T, Soutis C. Recent developments in advanced aircraft aluminium alloys. Mater Des (1980-2015). 2014;56:862–871.
[5] Fayomi J, Popoola API, Popoola OM, et al. Tribological and microstructural investigation of hybrid AA8011/ZrB2-Si3N4 nanomaterials for service life improvement. Results Phys. 2019;14:102469.
[6] Chen X, Peng Y, Peng S, et al. Flow and fracture behavior of aluminum alloy 6082-T6 at different tensile strain rates and triaxialities. PLoS One. 2017;12(7):e0181983.
[7] Verma S, Gupta M, Misra JP. In B. Katalinic, editor, Friction stir welding of aerospace materials Vienna, Austria: DAAAM International, 2016.
[8] Bahl S, Singh T, Kumar V, et al. A systematic review on recent progress in advanced joining techniques of lightweight materials. AIMS Mater Sci. 2021;8(1):62–81.
[9] Mehdi H, Mishra RS. Investigation of mechanical properties and heat transfer of welded joint of AA6061 and AA7075 using TIG + FSP welding approach. J Adv Join Process. 2020;1:100003.

[10] Mehdi H, Mishra RS. Effect of friction stir processing on mechanical properties and heat transfer of TIG welded joint of AA6061 and AA7075. Defence Technol. 2021; 17(3):715–727.
[11] Mehdi H, Mishra RS. Influence of friction stir processing on weld temperature distribution and mechanical properties of TIG-Welded joint of AA6061 and AA7075. Trans Indian Inst Met. 2020;73(7):1773–1788.
[12] Mishra RS, Mahoney MW, McFadden SX, et al. High strain rate superplasticity in a friction stir processed 7075 Al alloy. Scr Mater. 1999;42(2):163–168.
[13] Padhy GK, Wu CS, Gao SJ. Friction stir based welding and processing technologies - processes, parameters, microstructures and applications: a review. J Mater Sci Technol. 2018;34(1):1–38.
[14] Ma ZY. Friction stir processing technology: a review. Metall Mater Trans A. 2008;39(3): 642–658.
[15] Mabuwa S, Msomi V. Effect of friction stir processing on gas tungsten arc-welded and friction stir-welded 5083-H111 aluminium alloy joints. Adv Mater Sci Eng. 2019; 3510236:1–14.
[16] Mehdi H, Mishra RS. Study of the influence of friction stir processing on tungsten inert gas welding of different aluminum alloy. SN Appl Sci. 2019;1:712.
[17] Devireddy K, Devuri D, Cheepu MM, et al. Analysis of the influence of friction stir processing on gas tungsten arc welding of 2024 aluminum alloy weld zone. Int J Mech Prod Eng Res Dev. 2020;8(1):243–252.
[18] Mehdi H, Mishra RS. Effect of friction stir processing on microstructure and mechanical properties of TIG welded joint of AA6061 and AA7075. Metallogr Microstruct Anal. 2020;9(3):403–418.
[19] Barooni O, Abbasi M, Givi M, et al. New method to improve the microstructure and mechanical properties of joint obtained using FSW. Int J Adv Manuf Technol. 2017; 93(9–12):4371–4378.
[20] Shamanian M, Mostaan H, Safari M, et al. Friction stir modification of GTA 7075-T6 Al alloy weld joints: EBSD study and microstructural evolutions. Arch Civil Mech Eng. 2017;17(3):574–585.
[21] Kumar Rajak D, Pagar DD, Menezes PL, et al. Friction-based welding processes: friction welding and friction stir welding. J Adhes Sci Technol. 2020;34(24):2613–2637.
[22] Singh G, Kang AS, Singh K, et al. Experimental comparison of friction stir welding process and TIG welding process for 6082-T6 aluminium alloy. In: 5th international conference of materials processing and characterization (ICMPC), 2016, p. 3590–3600.
[23] Selvaraj G, Karthikeyan T, Mohanadass R, et al. Investigation on mechanical properties of welded aluminium joints of AA8011 using friction stir welding. Int J Appl Eng Res. 2015;10(13):11095–11100.
[24] Mehdi H, Mishra RS. An experimental analysis and optimization of process parameters of AA6061 and AA7075 welded joint by TIG + FSP welding using RSM. Adv Mater Process Technol. 2020;9:1–23.
[25] Ahmed N, Veeman L. Improvement of mechanical and microstructural properties of AA 5052-H32 TIG weldment using friction stir processing approach. J Mater Res Technol. 2022;19:332–344.
[26] Balakrishnan M, Dinaharan I, Palanivel R, et al. Effect of friction stir processing on microstructure and tensile behavior of AA6061/Al3Fe cast aluminium matrix composites. J Alloy Comp. 2019;785:531–541.
[27] Rahaman Hazari H, Balubai M, Suresh Kumar D, et al. Experimental investigation of TIG welding on AA 6082 and AA 8011. Mater Today. 2019;19(2):818–822.
[28] Giridharan K, Sevvel P, Senthilnathan K, et al. Experimental study on mechanical properties of friction stir welded dissimilar joints of aluminium alloys AA8011-AA6082. Int J Vehicle Struct Syst. 2019;11(2):135–139.

[29] Dawood HI, Mohammed KS, Rahmat A, et al. Effect of small tool pin profiles on microstructures and mechanical properties of 6061 aluminum alloy by friction stir welding. Trans Nonferrous Met Soc China 2015;25(9):2856–2865.
[30] Bahrami M, Besharati Givi MK, Dehghani K, et al. On the role of pin geometry in microstructure and mechanical properties of AA7075/SiC nano-composite fabricated by friction stir welding technique. Mater Des. 2014;53:519–527.
[31] AnandhaKumar CJ, Gopi S, Kumar SS, et al. Mechanical, metallurgical and tribological properties of friction stir processed aluminium alloy 6061 hybrid surface composites. Surf Topogr Metrol Prop. 2021;9(4):045019.
[32] Anandha Kumar CJ, Gopi S, Mohan DG, et al. Predicting the ultimate tensile strength and wear rate of aluminium hybrid surface composites fabricated via friction stir processing using computational methods. J Adhes Sci Technol. 2022;36(16):1707–1726.
[33] Sun Y, Tsuji N, Fujii H. Microstructure and mechanical properties of dissimilar friction stir welding between ultrafine grained 1050 and 6061-T6 aluminum alloys. Metals. 2016;6(10):249.
[34] Liu FC, Ma ZY. Influence of tool dimension and welding parameters on microstructure and mechanical properties of friction-stir-welded 6061-T651 aluminum alloy. Metall Mater Trans A. 2008;39(10):2378–2388.
[35] Rao KP, Ramanaiah N, Viswanathan N. Partially melted zone cracking in AA6061 welds. Mater Des. 2008;29(1):179–186.
[36] Mehdi H, Mishra RS. Effect of friction stir processing on mechanical properties and wear resistance of tungsten inert gas welded joint of dissimilar aluminum alloys. J Mater Eng Perform. 2021;30(3):1926–1937.
[37] Rao SRK, Reddy GM, Rao KP. Effects of thermo-mechanical treatments on mechanical properties of AA2219 gas tungsten arc welds. J Mater Process Technol. 2008;202(1–3): 283–289.
[38] Mathers G. The welding of aluminum and its alloys, 1st edn. Cambridge: Woodhead Publishing, 2002.
[39] Mehdi H, Mishra RS. Microstructure and mechanical characterization of tungsten inert gas-welded joint of AA6061 and AA7075 by friction stir processing. Proc Inst Mech Eng L. 2021;235(11):2531–2546.
[40] Khan NZ, Siddiquee AN, Khan ZA, et al. Investigations on tunneling and kissing bond defects in FSW joints for dissimilar aluminum alloys. J Alloys Compd. 2015;648: 360–367.
[41] Mabuwa S, Msomi V. The impact of submerged friction stir processing on the friction stir welded dissimilar joints. Mater Res Express. 2020;7(9):096513.
[42] Barbini A, Carstensen J, dos Santos JF. Influence of alloys position, rolling and welding directions on properties of AA2024/AA7050 dissimilar butt weld obtained by friction stir welding. Metals. 2018;8(4):202.
[43] Msomi V, Mabuwa S. Analysis of material positioning towards microstructure of the friction stir processed AA1050/AA6082 dissimilar joint. Adv. Industrial Manuf. Eng. 2020;1:100002.
[44] Kalemba-Rec I, Kopýsciánski M, Miara D, et al. Effect of process parameters on mechanical properties of friction stir welded dissimilar 7075-T651 and 5083-H111 aluminum alloys. Int J Adv Manuf Technol. 2018;97(5–8):2767–2779.
[45] Mastanaiah P, Sharma A, Reddy GM. Dissimilar friction stir welds in AA2219-AA5083 aluminium alloys: Effect of process parameters on material inter-mixing, defect formation, and mechanical properties. Trans Indian Inst Met. 2016;69(7):1397–1415.
[46] Hashmi AW, Mehdi H, Mishra RS, et al. Mechanical properties and microstructure evolution of AA6082/sic nanocomposite processed by Multi-Pass FSP. Trans Indian Inst Met. 2022;75(8):2077–2090.
[47] Mehdi H, Mishra RS. Modification of microstructure and mechanical properties of AA6082/ZrB2 processed by multipass friction stir processing. J Mater Eng Perform. 2022. https://doi.org/10.1007/s11665-022-07080-0.

[48] Mehdi H, Mishra RS. Mechanical properties and microstructure studies in friction stir welding (FSW) joints of dissimilar alloy- a review. J Achiev Mater Manuf Eng. 2016; 77(1):31–40.
[49] Mehdi, H, Mishra RS. Consequence of reinforced SiC particles on microstructural and mechanical properties of AA6061 surface composites by multi-pass FSP. J Adhes Sci Technol. 2022;36(12):1279–1298.
[50] Mehdi H, Mishra RS. Effect of multi-pass friction stir processing and SiC nanoparticles on microstructure and mechanical properties of AA6082-T6. Adv Ind Manuf Eng. 2021;3:100062.
[51] Smith WF, Hashemi J. Foundations of materials science and engineering, 4th ed. Boston, United States: McGraw-Hill, 2006.
[52] Mabuwa S, Msomi V. Comparative analysis between normal and submerged friction stir processed friction stir welded dissimilar aluminium alloy joints. J Mater Res Technol. 2020;9(5):9632–9644.
[53] Pandey C, Mahapatra MM, Kumar P, et al. Study on effect of double austenitization treatment on fracture morphology tensile tested nuclear grade P92 steel. Eng Fail Anal. 2019;96:158–167.